Deep Learning Assisted Linear Sampling Method for the Reconstruction of Perfect Electric Conductors

Shimoga Beerappa HARISHA, Erramshetty MALLIKARJUN, Magdum AMIT

Dept. of Electronics and Communication Engineering, National Institute of Technology, Farmagudi, Ponda, Goa, India

harishasb@jnnce.ac.in, emallikarjuna@nitgoa.ac.in, amitmagdum7671@gmail.com

Submitted September 21, 2023 / Accepted December 2, 2023 / Online first December 18, 2023

Abstract. *In this study, a linear approach, linear sampling method (LSM) is used to reconstruct the shape of perfectly electric conductors (PEC) with the help of deep learning as a post-processing technique. In microwave imaging, the LSM is a simple and reliable linear inversion technique for determining the morphological features of unknown objects under investigation. However, the output of this method depends on the frequency of operation, the choice of regularization parameter,and it is unable to produce satisfactory results for objects with complex shapes. To overcome this drawback, a deep learning approach is used in this work, which can produce a better output in terms of accuracy, resolution. Here, the rough estimate of the PEC scatterer obtained using LSM is used to train the U-Net based convolutional neural network, which maps this output with the corresponding ground truth profiles. The proposed hybrid model is validated using several examples of synthetic and experimental data.*

Keywords

Deep Learning, linear sampling method, PEC, microwave imaging

1. Introduction

Microwave imaging (MI) is a non-contact and non-invasive methodology to estimate concealed or implanted objects in a structure using electromagnetic waves in the microwave range. MI is widely used in medical imaging, non-destructive testing, geophysical explorations etc. [1], [2]. One of the challenges in microwave imaging is the reconstruction of perfectly electric conductors (PEC). The detection of PEC is essential in various applications, like concealed weapon detection [1–4], localization of metallic contaminants in food products [5] and landmine detection [6], [7] etc.

PEC reconstruction techniques are broadly classified as volume based and surface-based methods. A volume-based method, such as the local shape function, assigns a Boolean variable to each pixel to indicate whether it is PEC or not [8–10]. Genetic algorithms (GAs) are used to solve the PEC inverse scattering problem (ISP) in [11] and [12]. The main drawback of GA is that the computational cost increases exponentially with sample size [13]. In [14–16], a different volume-based approach for mixed targets that uses integral scattering equations in that each pixel has been given a complex permittivity value, and metallic objects have been modelled as dielectrics with a substantial but finite imaginary part. PEC scatterers are reconstructed by surface-based methods using the Newton-Kantorovich method [17], the Differential Evolution optimizer [18], [19], and the GAs [20–24]. The Level Set (LS) approach has been utilised successfully in [25] to produce the PEC contour without any prior knowledge of the scattering scenario. The subspace optimization method-based inversion process has been used to categorise each segment as PEC or non-PEC [26], [27].

LSM is one of the qualitative imaging procedures used for the shape reconstruction of dielectric as well as metallic targets. This method is rapid, reliable, and computationally efficient [28]. It has been applied for various applications like detection of coated objects, buried objects, objects behind walls, and breast cancer cells etc., [29–34]. LSM able to estimate applied by considering the targets to be either dielectric or perfect electric conducting (PEC) objects. The main drawback of this method is that the quality of output depends on frequency of operation and choice of regularization parameter [35], [36]. To overcome these limitations, a modified LSM indicator based on a multi-frequency approach is introduced. However, the improved results are inadequate. Hence, in this work, we propose another methodology based on deep-learning to tackle the above issues.

To the best of author's knowledge, there are very few literatures on the applicability of deep learning for the reconstruction of PEC objects [37]. An effective CNN-DL architecture is implemented through the modelling of the rough surface variation in terms of convenient spline type base functions. In [38], a deep learning-assisted linear sampling method (DLSM) is proposed for the reconstruction of multi-layered dielectric objects with cylindrical and rectangular cross-sections. The relative permittivity is randomly chosen from the interval [1], [5]. The background of the detection domain is assumed to be free space. So far, this is the only work reported on LSM with deep-learning. The novelty of

DOI: 10.13164/re.2024.0089

the paper lies in the proposed hybrid model, which combines conventional LSM and deep learning.Furthermore, the limitations of LSM, such as its output depending on the frequency of operation and the choice of regularization parameter, are also addressed using deep learning. Various examples of synthetic and experimental data sets [39] are used to validate the proposed model's performance. The results are excellent in terms of convergence rate and reconstruction quality.

This paper is organized as follows. The problem formulation is covered in Sec. 2, LSM algorithm is briefed in Sec. 2.1 and deep learning based linear sampling method for inverse problem of PEC is discussed in Sec. 2.2. Thereafter, numerical results for various testing examples are reported in Sec. 3. The effect of regularization parameter and frequency is discussed in Sec. 3.1 and 3.2, respectively. Finally, Section 4 contains the concluding remarks.

2. Problem Formulation

The paper considers a scenario involving two dimensional transverse magnetic (TM) characteristics and circular measurement configuration [40] as shown in Fig. 1.The unknown object is embedded within the investigation domain Ω.This object resides within a medium characterized by a homogeneous background.TM waves created by the N_{tx} number of transmitting antennas denoted as T_{x}, illuminate the unknown scatterers. The scattered field is measured by the N_{rx} number of receiving antennas denoted as R_{x}.

The integral equations for the relationship between scattered fields and the induced currents are as follows [41], [42]:

$$u\left(\underline{r}\right) = u^{\mathrm{inc}}\left(\underline{r}\right) - \mathrm{j}\omega\mu_{\mathrm{b}} \int_{\mathrm{PEC}} G\left(\underline{r}, \underline{t}'\right) I^{\mathrm{c}}\left(\underline{t}'\right) \mathrm{d}\underline{t}', \quad \underline{t}' \in \partial\pi, \underline{r} \in \partial\pi, \tag{1}$$

$$u^{\mathrm{scat}}\left(\underline{r}\right) = -\mathrm{j}\omega\mu_{\mathrm{b}} \int_{\mathrm{PEC}} G\left(\underline{r}, \underline{t}'\right) I^{\mathrm{c}}\left(\underline{t}'\right) \mathrm{d}\underline{t}', \quad \underline{t}' \in \partial\pi, \quad \underline{r} \in \Gamma. \tag{2}$$

The incident field, the scattered field, and the total field are denoted by u^{inc}, u^{scat}, and u, respectively. $\underline{r}, \underline{t}' \in (x, y)$ are spatial variables that indicate the Cartesian coordinates of the receivers and emitter, respectively. ϵ_{b} denotes the background's permittivity, μ_{b} denotes the magnetic permeability, and ω denotes the working frequency. I^{c} is the impressed conduction current density. I^{c} is related to the boundary conditions of PEC. For PEC objects, the scattered fields depend on the object's shape and wave's frequency.

The free space Green's function is denoted by $G\left(\underline{r}, \underline{t}'\right)$ and defined as

$$G\left(\underline{r}, \underline{t}'\right) = \frac{1}{4\mathrm{j}} H_0^{(2)}\left(k_{\mathrm{b}}\left|\underline{r} - \underline{t}'\right|\right) \tag{3}$$

where $H_0^{(2)}(.)$ is the Hankel function of second kind and zeroth order and k_{b} is the wave number. In PEC, the induced currents are present only at the boundary $\partial\pi$.

The solution to (1) and (2) can be found by applying the method of moments to transform them into discrete matrix equations by discretizing the integral equations and then calculating unknown I^{c} and u^{scat}. The related mathematical details can be found in [41], [42].

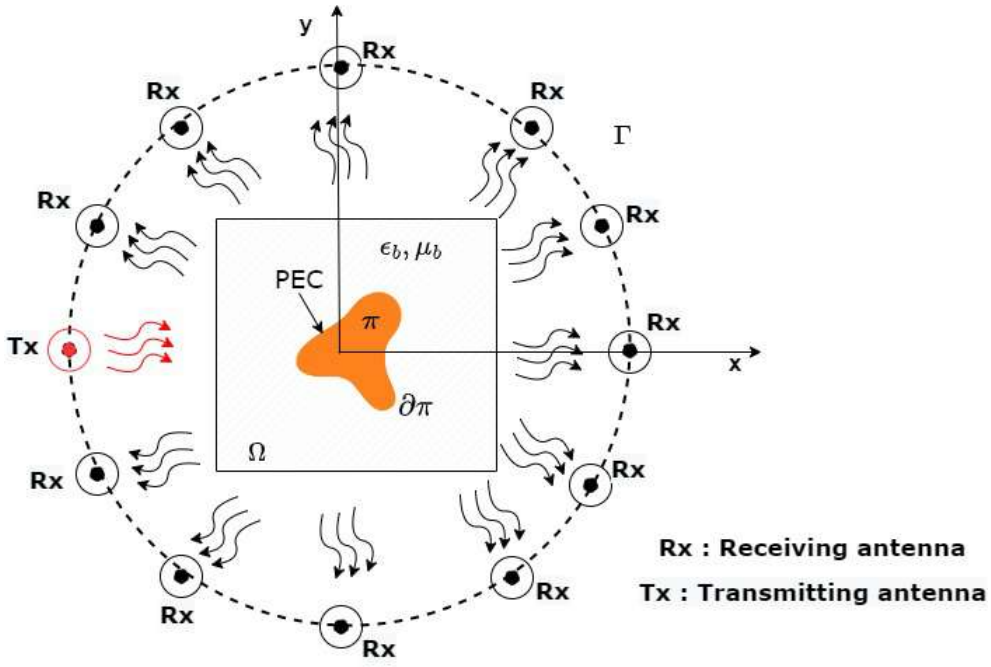

Fig. 1. Two-dimensional measurement configuration.

2.1 Linear Sampling Method

The LSM provides an estimate of the targets support by solving an auxiliary linear inverse problem rather than the nonlinear one formulated through (1) and (2). With respect to the scenario described above, the auxiliary problem is cast as [43]

$$\mathcal{F}[\xi] = \int_0^{2\pi} u^{\text{scat}}\left(\underline{r}, \theta\right) \xi\left(\underline{r}_{\text{s}}, \theta\right) \mathrm{d}\theta = G\left(\underline{r}, \underline{r}_{\text{s}}\right) \quad (4)$$

where G is the point source, $\underline{r}_{\text{s}} \in \Omega$ denotes a point of an arbitrary grid that samples the region under test Ω , ξ is the unknown to be determined and $\mathcal{F} : L^2(\Gamma) \rightarrow L^2(\Gamma)$ is the far-field operator [8].

Due to compactness of $\mathcal{F}$, equation (4) corresponds to a linear ill-posed inverse problem [43]. Hence, a stable solution of (4) in the generic sampling point requires regularization. Usually, this is done by considering the Tikhonov regularization, and singular value decomposition (SVD), the final form of solution is

$$\xi\left(\underline{r}_{\text{s}}, \theta\right) = \sum_{n=1}^{\infty} \frac{\lambda_n}{\lambda_n^2 + \alpha^2} \left\langle G\left(\underline{r}, \underline{r}_{\text{s}}\right), u_n(\underline{r}) \right\rangle_{\Gamma} v_n(\theta) \quad (5)$$

where $\{\mu_n, \lambda_n, v_n\}$ denotes SVD of $\mathcal{F}$ and α is the Tikhonov parameter / regularization parameter.

The estimated support is achieved by evaluating the energy (i.e., the L^2 norm) of ξ, $\forall\ \underline{r}_{\text{s}} \in \Omega$, as this assumes its lowest values in the points of the investigated region belonging to the target, while it diverges in points external to it [43]. Therefore, the support is simply determined by plotting the LSM indicator over Ω and associating the sampling points where the indicator is low to the unknown objects.

From (5), one achieves the explicit expression of the LSM indicator

$$\begin{aligned} \Upsilon\left(\underline{r}_{\text{s}}\right) &= \int_{\Gamma} \left|\xi\left(\underline{r}_{\text{s}}, \theta\right)\right|^2 \mathrm{d}\theta \\ &= \sum_{n=1}^{\infty} \left(\frac{\lambda_n}{\lambda_n^2 + \alpha^2}\right)^2 \left\| \left\langle G\left(\underline{r}, \underline{r}_{\text{s}}\right), u_n(\underline{r}) \right\rangle \right\|_{\Gamma}^2 \end{aligned} \quad (6)$$

whose evaluation is computationally straightforward as it requires a single evaluation of the SVD of $\mathcal{F}$. Moreover, the Tikhonov parameter can be determined only once for all sampling points [44–47]. The regularization parameter employed in this proposed technique is the same for all sampling points and is set in accordance with the physics-based criteria described in [31], which eliminates the need to understand the level of noise present in the observed data. Regularization parameter is set as $\alpha = 0.0001\lambda_1$, where λ_1 is the leading singular value.

2.2 Deep Learning Assisted Linear Sampling Method for Inverse Problem of PEC

In recent years, deep learning has become one of the most powerful methods in the field of regression and classification problems. These methods are much faster and produce better image quality compared to the conventional iterative methods based on optimization [48]. With a powerful nonlinear matching ability and a one-step testing procedure, deep learning methods are becoming the most popular to use in microwave imaging techniques to obtain an inverse solution in real-time.

U-Net is one of the encoder-decoder CNN architecture used exclusively for image segmentation [49]. U-Net has proven its effectiveness in biomedical image segmentation [49], [50] and permittivity estimation [51].The recent works published in this area [38, 51–55] show that the U-Net is well-suited for solving EISPs along with backpropagation, contrast source inversion, SVBIM, etc.

In this regard, U-Net architecture having an encoder depth of 3 is used in the proposed model. The Proposed scheme for embedding deep learning in LSM is as shown in Fig. 2. The detail of the U-Net architecture with an encoder depth of 3 is as shown in Fig. 2(a). Since the U-Net architecture was originally designed for segmentation, it is modified such that the Softmax layer is removed and the segmentation layer is replaced with a regression layer. It consists of 3×3 convolutional, rectified linear units (ReLU) and 2×2 a max-pooling layers (contraction path), followed by successive up sampling and convolutional layers (expansion path). Additionally, in the expansive path, there are three concatenations with the corresponding feature maps from the contracting path. The purpose of this path is to combine precise localization with contextual information from the contracting path. More details about U-Net can be found in [49].

2.3 Training and Testing of the Network

The schematic for training and testing U-Net architecture is as shown in Fig. 2(b) and Fig. 2(c), respectively. The initial contrast function derived by solving LSM is used to train the U-Net with true contrast as the network's target (label). The training data contains 11600 reference PEC objects of various shapes like circular cylinders, rectangle, L shape, T shape, E shape, F shape, H shape and U shape PEC objects. The DOI is discretized into 40×40 small square cells. The background of the detection domain is assumed to be free space (contrast function is set to zero). The learning rate determines the step size during optimization. If the learning rate is excessively high, it can cause rapid convergence or divergence, while a very low learning rate may lead to slow convergence or getting stuck in local minima [56]. Empirically, we have set the learning rate at 0.0001.The batch size determines the number of samples used in each iteration of training. Larger batch sizes can expedite the training process, but if they are too large, they may result in out-of-memory errors. Based on the recommendation in [57] and considering the dataset size of 11600, we have chosen a batch size of 40 (batch size $\times$ no. of iterations = total no. of training data). The number of epochs represents how many times the model goes through the entire training dataset. Too few epochs may result in underfitting, while too many may lead

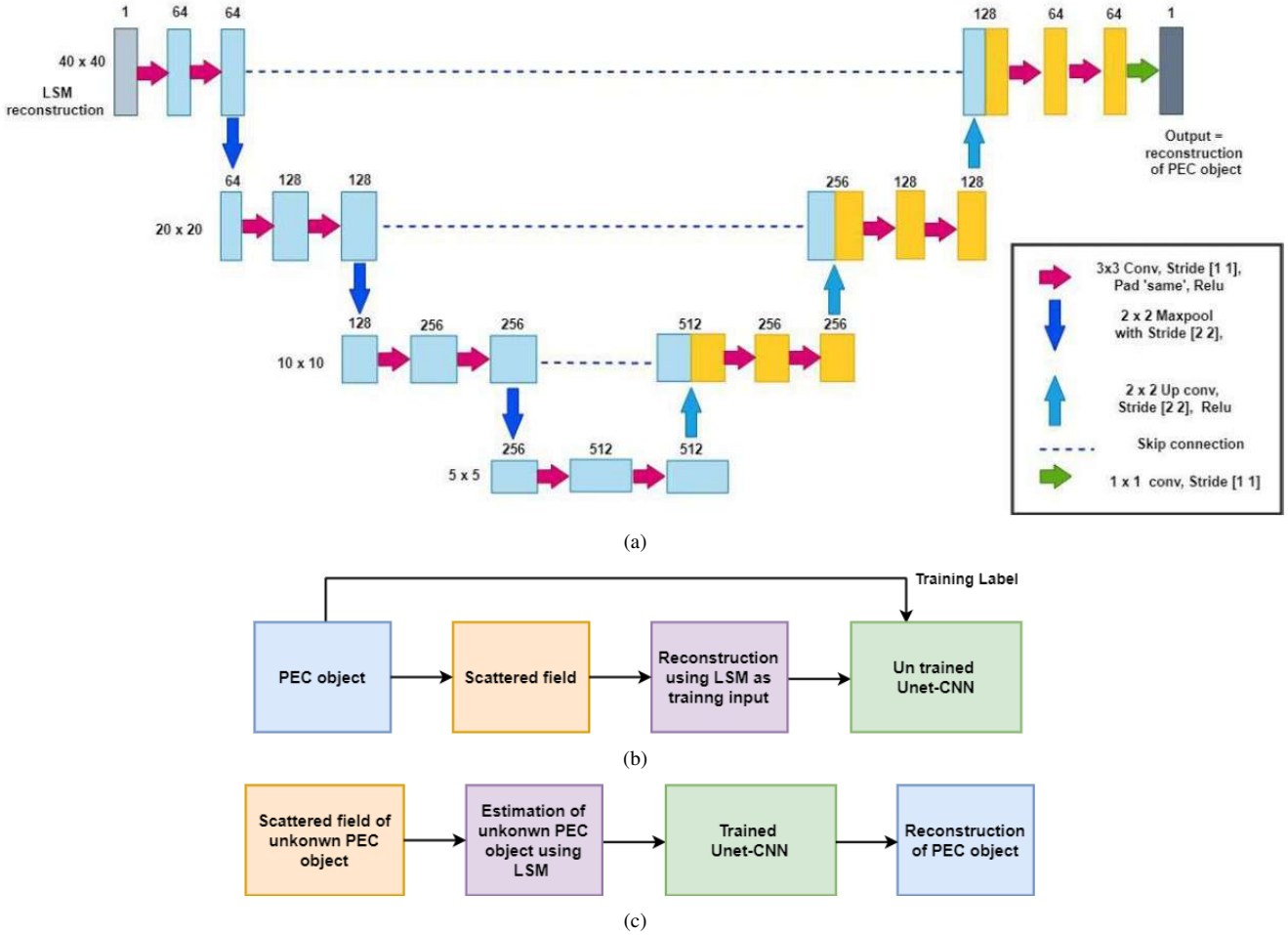

Fig. 2. (a) Architecture details of U-Net for the proposed model. (b) Training the CNN using LSM reconstruction as input. (c) Reconstruction of PEC objet using LSM and U-Net-CNN.

to overfitting [56]. It has been observed during training that after the 28th epoch, the loss function saturates; therefore, we have chosen to set the number of epochs at 30. Elapsed time for training is 206 minutes 30 seconds in a personal computer with CPU: 12th Gen Intel(R) Core(TM) i7-12700 2.10 GHz and 16 GB RAM. The U-Net learns the relationship between input and output by updating network's weight matrix and bias. The trained U-Net is tested using the contrast function obtained by the scattered field of the unknown PEC objects. Priori information about the PEC scatterer like approximate position, size etc., is not required for this approach. In the reconstructed result, negative values are made zero as post processing (background of DOI is free space). The various results of testing are discussed in the subsequent section.

3. Results and Discussion

The imaging setup consists of a square investigation domain of side 20 cm × 20 cm. PEC objects are reconstructed using the noisy scattered field. MATLAB's Deep Learning toolbox is used to build the U-Net architecture. The proposed scheme is tested for various test images. Here 24 transceivers are used, which are located uniformly on a circular measurement domain of 0.6 m radius. The operating frequency is 3 GHz. The scattered field of synthetic data have been corrupted with additive Gaussian noise at the level of a signal-to-noise ratio (SNR) of 30 dB.The proposed scheme is tested for the various letters shaped PEC objects and the reconstruction results for some representative examples are shown in Figs. 3–8. The results reveal that the suggested method outperforms the LSM algorithm in reconstructing high-quality images.

Example 1: Consists of circular and rectangular cylinders.

Example 2: Consists of L and T shape objects with two arms.

Example 3: Consists of U, H and F shape objects with three arms.

Example 4: Consists of E-shape objects with four arms.

Example 5: Consists of U and rectangular shape objects of Fresnel experimental data.

3.1 Example 1: Consists of Circular and Rectangular Cylinders

A PEC circular cylinder of radius 3.5 cm centred at (3 cm,–2 cm) as shown in Fig. 3(a) is considered. The reconstruction result of LSM is shown in Fig. 3(b). This is given as input to the trained CNN and the corresponding output is as shown in Fig. 3(c). As the object is placed in a free space, the contrast function for background is zero and cannot be negative. So, as a post processing, any value less than 0.3 is set to 0 and the corresponding result is shown in Fig. 3(d). For rest of the examples, the post processed output is shown as there is no much difference in the object shape and location.

The rectangular strip of width 7.5 cm and height of 5.0 cm is positioned as shown in Fig. 4(a). The reconstruction result of LSM and CNN is as shown in Fig. 4(b) and 4(c), respectively. The LSM reconstruction looks like circular objects as sharp corners are rounded. Whereas, proposed method conserves the sharp corners and reconstruct the correct shape and size.

3.2 Example 2: Consists of L and T Shape Objects with Two Arms

In this study, a L-shape object is taken having both arm's length and breadth of 9.5 cm and 2.5 cm, respectively, positioned as shown in Fig. 5(a). The reconstruction result of LSM and CNN is as shown in Fig. 5(b) and 5(c), respectively. A T-shape object having both arm's length and breadth of 7.0 cm and 2.0 cm, respectively, positioned as shown in Fig. 5(d). The reconstruction result of LSM and CNN is as shown in Fig. 5(e) and 5(f), respectively. In LSM, the internal sharp corner is severely rounded and cannot reconstruct the correct shape and size of the object. However, the CNN result recovers the internal sharp covers and is able to identify the shape and size more accurately.

3.3 Example 3 : Consists of U, H and F Shape Objects with Three Arms

A U-shape object having both arm's length and breadth of 10.0 cm and 6.0 cm ,respectively, positioned as shown in Fig. 6(a). The reconstruction result of LSM and CNN is as shown in Fig. 6(b) and 6(c), respectively. A H-shape object having both arm's length and breadth of 8.5 cm and 7.5 cm, respectively, positioned as shown in Fig. 6(d). The reconstruction result of LSM and CNN is as shown in Fig. 6(e) and 6(f), respectively. A F-shape object having both arm's length and breadth of 10.0 cm and 5.0 cm, respectively, positioned as shown in Fig. 6(g). The reconstruction result of LSM and CNN is as shown in Fig. 6(h) and 6(i), respectively. In letter U, F and H, the reconstruction of internal edges is relatively thin due to multiple scattering effects. However, the shape can be approximated.

3.4 Example 4 : Consists of E Shape Objects with Four Arms

A E-shape object having both arm's length and breadth of 8.0 cm and 14.0 cm, respectively, positioned as shown in Fig. 7(a). The reconstruction result of LSM and CNN is as shown in Fig. 7(b) and 7(c), respectively.The reconstruction of internal edges in an E-shaped object is comparatively thin due to multiple scattering effects since its size and arms are larger than in Example 3. However, it's possible to fairly estimate the shape.

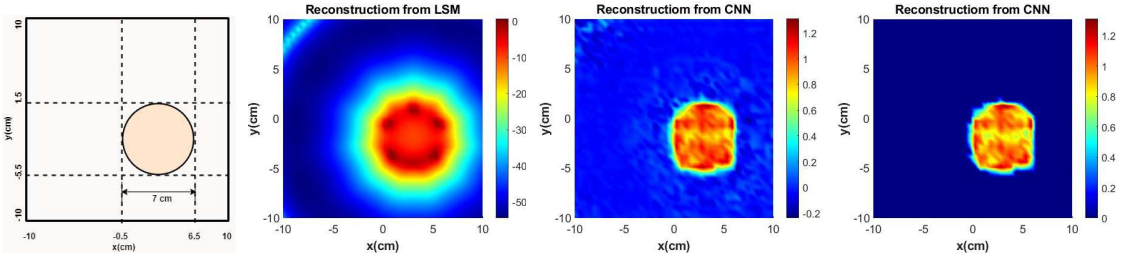

(a) Reference profile (b) LSM (c) Output of CNN (d) Post processed result of CNN

Fig. 3. Reconstruction results for circular cylinder PEC object.

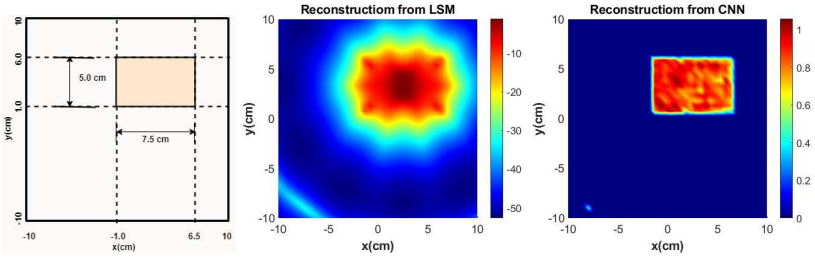

(a) Reference profile (b) LSM reconstruction (c) Post processed result of CNN

Fig. 4. Reconstruction results for rectangular shape PEC object.

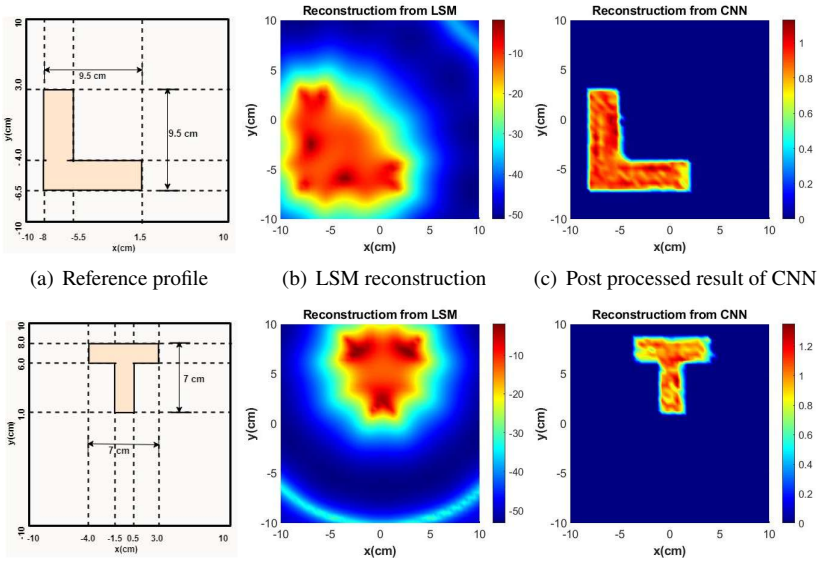

(a) Reference profile (b) LSM reconstruction (c) Post processed result of CNN

(d) Reference profile (e) LSM reconstruction (f) Post processed result of CNN

Fig. 5. Reconstruction results for example 2 PEC object. L shape object in (a)–(c) and T shape object in (d)–(f).

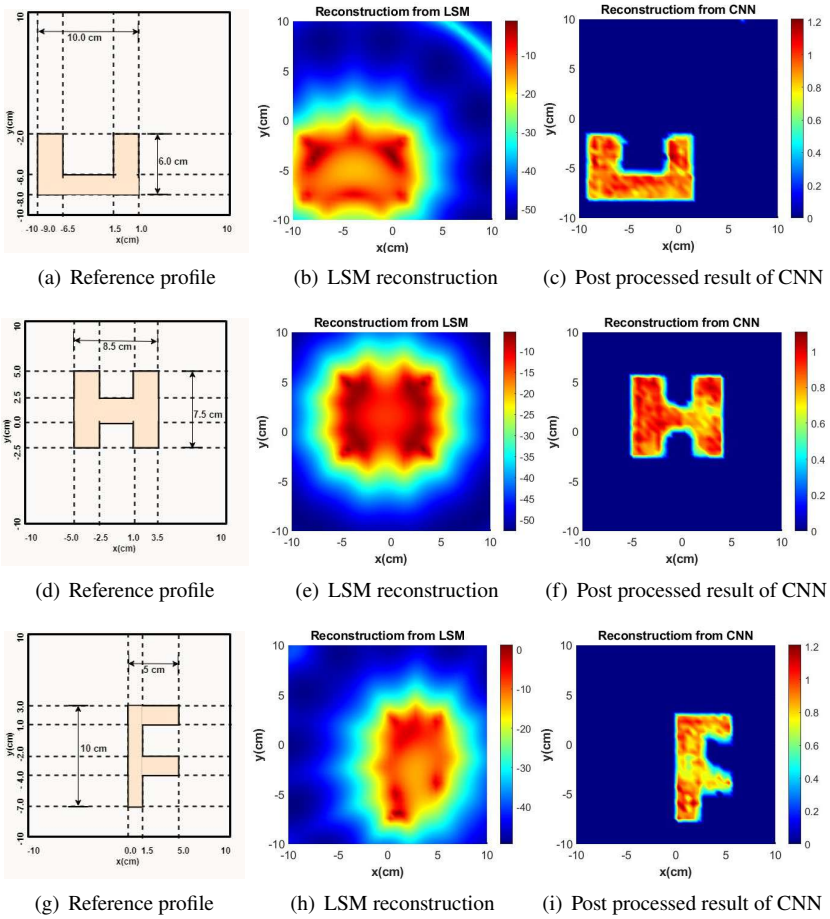

(a) Reference profile (b) LSM reconstruction (c) Post processed result of CNN

(d) Reference profile (e) LSM reconstruction (f) Post processed result of CNN

(g) Reference profile (h) LSM reconstruction (i) Post processed result of CNN

Fig. 6. Reconstruction results for example 3 PEC objects.

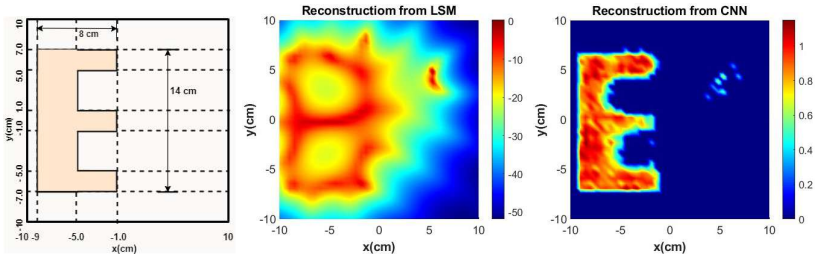

(a) Reference profile (b) LSM reconstruction (c) Post processed result of CNN

Fig. 7. Reconstruction results for example 4 PEC object.

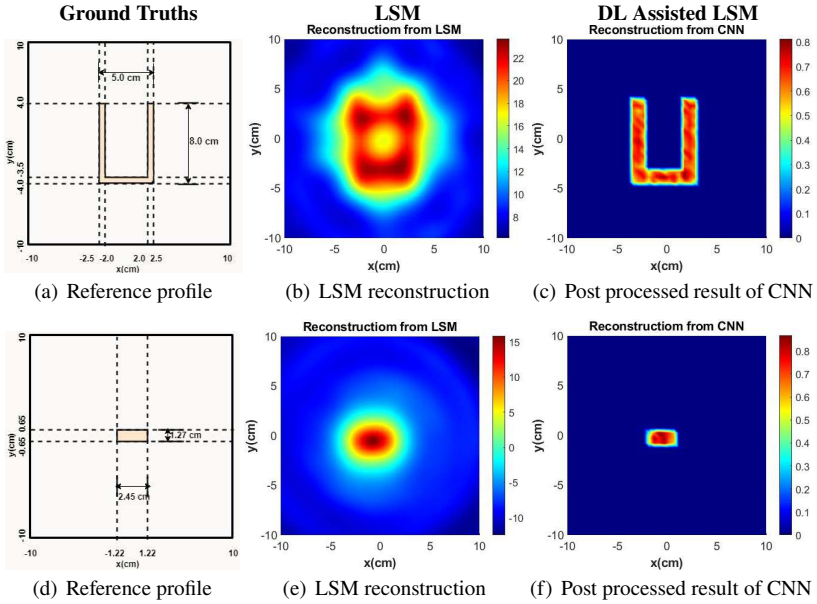

(a) Reference profile (b) LSM reconstruction (c) Post processed result of CNN

(d) Reference profile (e) LSM reconstruction (f) Post processed result of CNN

Fig. 8. Reconstruction results for example 5 PEC object.

3.5 Example 5 : Consists of U Shape and Rectangular Objects of Fresnel Experimental Data

The objects were sequentially illuminated at $0°, 10°, 20°, \ldots, 350°$ in steps of $10°$, and the scattered fields were measured from $60°, 65°, 70°, \ldots, 300°$ in steps of $5°$. Operating frequency considered here is 4 GHz [41].

A U-shape object having both arm's length and breadth of 5.0 cm and 8.0 cm, respectively, positioned as shown in Fig. 8(a). The reconstruction result of LSM and CNN is as shown in Fig. 8(b) and 8(a), respectively. A rectangular object having both arm's length and breadth of 2.45 cm and 1.27 cm, respectively, positioned as shown in Fig. 8(d). The reconstruction result of LSM and CNN is as shown in Fig. 8(e) and 8(f), respectively.

In summary, it has been shown that the proposed method can successfully reconstruct the shape of the more complex PEC objects. The proposed method can be more effectively recover some geometrical aspects that can't be faithfully restored using the traditional LSM method.

3.6 Effect of Regularization Parameter

The main drawback of the LSM is that the quality of output depends on the choice of regularization parameter [35], [36]. To overcome this limitation, a multiple regularization parameter approach is used, where the CNN is trained using LSM reconstructed results obtained at various regularization parameters like $\alpha = 0.1\lambda_1, 0.01\lambda_1, 0.001\lambda_1$ and $0.0001\lambda_1$, where λ_1 is the leading singular value. The trained CNN is tested for various PEC profiles like L-shape, T-shape and U-shape. The reconstruction result by LSM and CNN at various regularization parameters is as shown in Figs. 9–11. From the result, it can be concluded that, firstly, although the training is done at regularization parameters $\alpha = 0.1\lambda_1, 0.01\lambda_1, 0.001\lambda_1$ and $0.0001\lambda_1$, the reconstruction results at $\alpha = 0.1547\lambda_1, 0.0786\lambda_1$ and $0.0561\lambda_1$ are also satisfactory, indicating the robustness and generalization of the proposed method. Secondly, the LSM fails to reconstruct at certain regularization parameters, but the deep learning-assisted LSM can recover satisfactorily at various untrained regularization parameters.

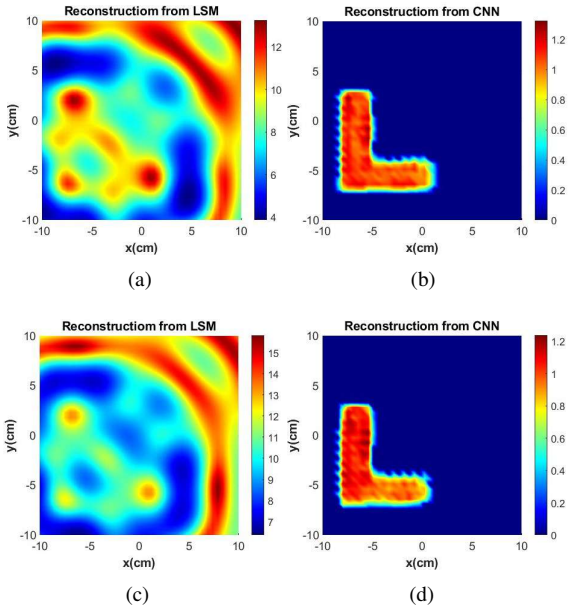

Fig. 9. Reconstruction of L-shape PEC object as shown in Example 2, Fig. 5(a), by LSM and CNN at regularization parameter $\alpha = 0.1\lambda_1$ and $\alpha = 0.1547\lambda_1$.

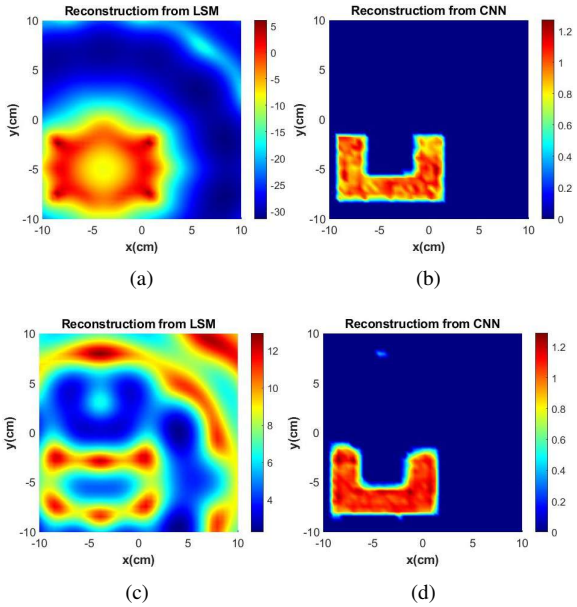

Fig. 10. Reconstruction of U-shape PEC object as shown in Example 3, Fig. 6(a), by LSM and CNN at regularization parameter $\alpha = 0.001\lambda_1$ and $\alpha = 0.7867\lambda_1$.

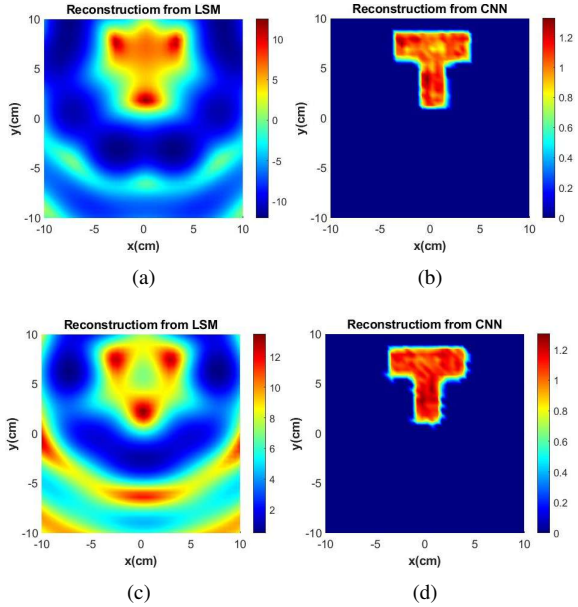

Fig. 11. Reconstruction of T-shape PEC object as shown in Example 2, Fig. 5(d), by LSM and CNN at regularization parameter $\alpha = 0.01\lambda_1$ and $\alpha = 0.0567\lambda_1$.

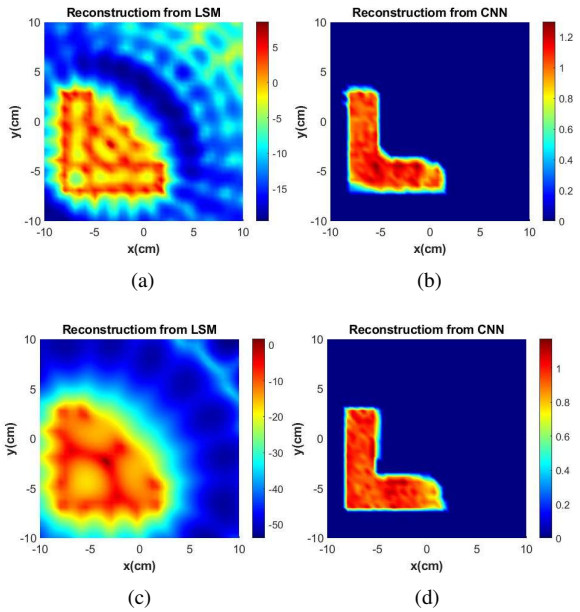

Fig. 12. Reconstruction of L-shape PEC object as shown in Example 2, Fig. 5(a), by LSM and CNN at 8 GHz and 4 GHz.

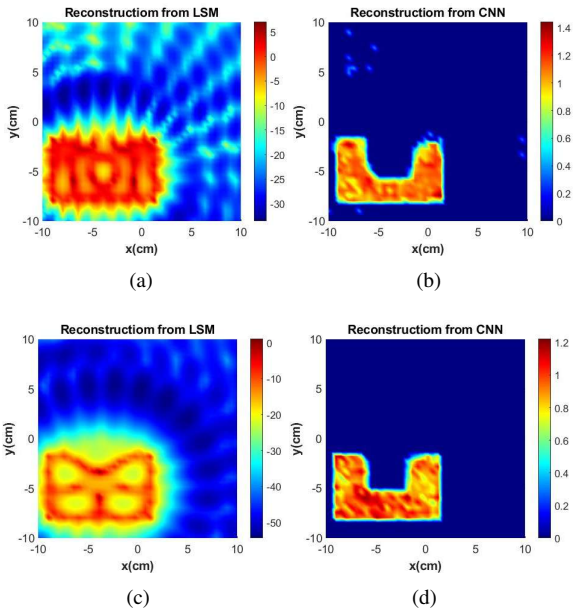

Fig. 13. Reconstruction of U-shape PEC object as shown in Example 3, Fig. 6(a), by LSM and CNN at 8 GHz and 6 GHz.

3.7 Effect of Frequency

The reconstruction quality of the LSM deteriorates at higher frequencies. To overcome this limitation, a multiple frequency approach is used, where the CNN is trained with LSM reconstructions obtained at multiple frequencies like 1 GHz, 3 GHz, 5 GHz and 7 GHz. The trained CNN is tested for PEC profiles like L-shape and U-shape. The reconstruction result by LSM and CNN at various frequencies is as shown in Figs. 12 and 13. The two observations can be made from the result. Firstly, although the training is done 1 GHz, 3 GHz, 5 GHz and 7 GHz, the reconstruction results at 4 GHz and 8 GHz is also satisfactory indicating the robustness and generalization of the proposed method. Secondly, the LSM fails to reconstruct at higher frequencies but deep learning assisted LSM can recover satisfactorily also at higher frequencies.

4. Conclusion

In this paper, a deep learning based LSM approach is introduced to reconstruct perfectly electric conductors. In this work, U-Net CNN architecture is used where an initial guess by the LSM is fed to CNN. The network is trained by generating the reference profiles of circular cylinders, rectangle, L shape, T shape, E shape; F shape, H shape and U shape PEC objects. Thereafter, this trained model is tested on various examples including synthetic and experimental data sets. It is also found that the proposed scheme outperforms conventional LSM in terms of frequency of operation and choice of regularization parameter. A more advanced architecture can yield even better results, which will be explored in our subsequent studies.

Acknowledgments

The research work carried out in this paper is supported by the Core Research Grant, SERB, India, File no. CRG/2020/004127.

References

[1] LIU, T., ZHAO, Y., WEI, Y., et al. Concealed object detection for activate millimeter wave image. *IEEE Transactions on Industrial Electronics*, 2019, vol. 66, no. 12, p. 9909–9917. DOI: 10.1109/TIE.2019.2893843

[2] BRIQECH, Z., GUPTA, S., BELTAY, A. A., et al. 57-64 GHz imaging/detection sensor-part II: Experiments on concealed weapons and threatening materials detection. *IEEE Sensors Journal*, 2020, vol. 20, no. 18, p. 10833–10840. DOI: 10.1109/JSEN.2020.2997293

[3] ZHURAVLEV, A., RAZEVIG, V., CHIZH, M., et al. A new method for obtaining radar images of concealed objects in microwave personnel screening systems. *IEEE Transactions on Microwave Theory and Techniques*, 2021, vol. 69, no. 1, p. 357–364. DOI: 10.1109/TMTT.2020.3023443

[4] WANG, C., SHI, J., ZHOU, Z., et al. Concealed object detection for millimeter-wave images with normalized accumulation map. *IEEE Sensors Journal*, 2021, vol. 21, no. 5, p. 6468–6475. DOI: 10.1109/JSEN.2020.3040354

[5] OK, G., KIM, H. J., CHUN, H. S., et al. Foreign-body detection in dry food using continuous sub-terahertz wave imaging. *Food Control*, 2014, vol. 42, p. 284–289. DOI: 10.1016/j.foodcont.2014.02.021

[6] BOURGEOIS, J. R., SMITH, G. S. A complete electromagnetic simulation of the separated aperture sensor for detecting buried land mines. *IEEE Transactions on Antennas and Propagation*, 1998, vol. 46, no. 10, p. 1419–1426. DOI: 10.1109/8.725272

[7] BANSAL, R. Of mice and men [Microwave surfing]. *IEEE Microwave Magazine*, 2015, vol. 16, no. 11, p. 18–20. DOI: 10.1109/MMM.2015.2478088

[8] CHEW, W. C., OTTO, G. P. Microwave imaging of multiple conducting cylinders using local shape functions. *IEEE Microwave and Guided Wave Letters*, 1992, vol. 2, no. 7, p. 284–286. DOI: 10.1109/75.143396

[9] WEEDON, W. H., CHEW, W. C. Time-domain inverse scattering using the local shape function (LSF) method. *Inverse Problems*, 1993, vol. 9, no. 5, p. 551–564. DOI: 10.1088/0266-5611/9/5/005

[10] OTTO, G. P., CHEW, W. C. Microwave inverse scattering-local shape function imaging for improved resolution of strong scatterers. *IEEE Transactions on Microwave Theory and Techniques*, 1994, vol. 42, no. 1, p. 137–141. DOI: 10.1109/22.265541

[11] ZHOU, Y., LING, H. Electromagnetic inversion of IPswich objects with the use of the genetic algorithm. *Microwave and Optical Technology Letters*, 2002, vol. 33, no. 6, p. 457–459. DOI: 10.1002/mop.10349

[12] TAKENAKA, T., MENG, Z. Q., TANAKA, T., et al. Local shape function combined with genetic algorithm applied to inverse scattering for strips. *Microwave and Optical Technology Letters*, 1997, vol. 16, no. 6, p. 337–341. DOI: 10.1002/(SICI)1098-2760(19971220)16:6<337::AID-MOP5>3.0.CO;2-L

[13] QING, A. Microwave imaging of parallel perfectly conducting cylinders. *International Journal of Imaging Systems and Technology*, 2001, vol. 11, no. 6, p. 365–371. DOI: 10.1002/ima.10000

[14] YU, C., SONG, L. P., LIU, Q. H. Inversion of multi-frequency experimental data for imaging complex objects by a DTA-CSI method. *Inverse Problems*, 2005, vol. 21, no. 6, p. 165–178. DOI: 10.1088/0266-5611/21/6/S12

[15] AZARO, R., DONELLI, M., FRANCESCHINI, D., et al. Multiscaling reconstruction of metallic targets from TE and TM experimental data. *Microwave and Optical Technology Letters*, 2006, vol. 48, no. 2, p. 322–324. DOI: 10.1002/mop.21338

[16] SUN, S., KOOIJ, B. J., YAROVOY, A. G. A linear model for microwave imaging of highly conductive scatterers. *IEEE Transactions on Microwave Theory and Techniques*, 2018, vol. 66, no. 3, p. 1149–1164. DOI: 10.1109/TMTT.2017.2772795

[17] ROGER, A. Newton-Kantorovitch algorithm applied to an electromagnetic inverse problem. *IEEE Transactions on Antennas and Propagation*, 1981, vol. 29, no. 2, p. 232–238. DOI: 10.1109/TAP.1981.1142588

[18] QING, A. Electromagnetic inverse scattering of multiple two-dimensional perfectly conducting objects by the differential evolution strategy. *IEEE Transactions on Antennas and Propagation*, 2003, vol. 51, no. 6, p. 1251–1262. DOI: 10.1109/TAP.2003.811492

[19] QING, A. Electromagnetic inverse scattering of multiple perfectly conducting cylinders by differential evolution strategy with individuals in groups (GDES). *IEEE Transactions on Antennas and Propagation*, 2004, vol. 52, no. 5, p. 1223–1229. DOI: 10.1109/TAP.2004.827495

[20] CHIU, C. C., LIU, P. T. Image reconstruction of a perfectly conducting cylinder by the genetic algorithm. *IEE Proceedings - Microwaves, Antennas and Propagation*, 1996, vol. 143, no. 3, p. 249–253. DOI: 10.1049/ip-map:19960363

[21] CHIEN, W., HUANG, C. H., CHIU, C. C. Cubic-spline expansion for a two-dimensional periodic conductor in free space. *International Journal of Applied Electromagnetics and Mechanics*, 2006, vol. 24, no. 1–2, p. 105–114. DOI: 10.3233/jae-2006-780

[22] CHIEN, W., CHIU, C. C., LI, C. L. Cubic-spline expansion for a conducting cylinder buried in a slab medium. *Electromagnetics*, 2006, vol. 26, no. 5, p. 329–343. DOI: 10.1080/02726340600710783

[23] ZHOU, Y., LI, J., LING, H. Shape inversion of metallic cavities using hybrid genetic algorithm combined with tabu list. *Electronics Letters*, 2003, vol. 39, no. 3, p. 280–281. DOI: 10.1049/el:20030207

[24] CHIEN, W., CHIU, C. C. Using NU-SSGA to reduce the searching time in inverse problem of a buried metallic object. *IEEE Transactions on Antennas and Propagation*, 2005, vol. 53, no. 10, p. 3128–3134. DOI: 10.1109/TAP.2005.856362

[25] LITMAN, A., LESSELIER, D., SANTOSA, F. Reconstruction of a two-dimensional binary obstacle by controlled evolution of a level-set. *Inverse Problems*, 1998, vol. 14, no. 3, p. 685–706. DOI: 10.1088/0266-5611/14/3/018

[26] YE, X. Z., ZHONG, Y., CHEN, X. Reconstructing perfectly electric conductors by the subspace-based optimization method with continuous variables. *Inverse Problems*, 2011, vol. 27, no. 5, p. 1–14. DOI: 10.1088/0266-5611/27/5/055011

[27] SHEN, J., ZHONG, Y., CHEN, X., et al. Inverse scattering problems of reconstructing perfectly electric conductors with TE illumination. *IEEE Transactions on Antennas and Propagation*, 2013, vol. 61, no. 9, p. 4713–4721. DOI: 10.1109/TAP.2013.2271891

[28] COLTON, D., KIRSCH, A. A simple method for solving inverse scattering problems in the resonance region. *Inverse Problems*, 1996, vol. 12, no. 4, p. 383–39. DOI: 10.1088/0266-5611/12/4/003

[29] COLTON, D., MONK, P. Target identification of coated objects. *IEEE Transactions on Antennas and Propagation*, 2006, vol. 54, no. 4, p. 1232–1242. DOI: 10.1109/TAP.2006.872564

[30] CATAPANO, I., CROCCO, L., ISERNIA, T. Improved sampling methods for shape reconstruction of 3-D buried targets. *IEEE Transactions on Geoscience and Remote Sensing*, 2008, vol. 46, no. 10, p. 3265–3273. DOI: 10.1109/TGRS.2008.921745

[31] CATAPANO, I., CROCCO, L. An imaging method for concealed targets. *IEEE Transactions on Geoscience and Remote Sensing*, 2009, vol. 47, no. 5, p. 1301–1309. DOI: 10.1109/TGRS.2008.2010773

[32] CATAPANO, I., SOLDOVIERI, F., CROCCO, L. On the feasibility of the linear sampling method for 3-D GPR surveys. *Progress In Electromagnetics Research*, 2011, vol. 118, p. 185–203. DOI: 10.2528/PIER11042704

[33] CATAPANO, I., CROCCO, L. A qualitative inverse scattering method for through-the-wall imaging. *IEEE Geoscience and Remote Sensing Letters*, 2010, vol. 7, no. 4, p. 685–689. DOI: 10.1109/LGRS.2010.2045473

[34] BOZZA, G., BRIGNONE, M., PASTORINO, M. Application of the no-sampling linear sampling method to breast cancer detection. *IEEE Transactions on Antennas and Propagation*, 2010, vol. 57, no. 10, p. 2525–2534. DOI: 10.1109/TBME.2010.2055059

[35] SUN, J. An eigenvalue method using multiple frequency data for inverse scattering problems. *Inverse Problems*, 2012, vol. 28, no. 2, p. 1–15. DOI: 10.1088/0266-5611/28/2/025012

[36] GUZINA, B., CAKONI, F., BELLIS, C. On the multi-frequency obstacle reconstruction via the linear sampling method. *Inverse Problems*, 2010, vol. 26, no. 12, p. 1–29. DOI: 10.1088/0266-5611/26/12/125005

[37] AYDIN, I., BUDAK, G., SEFER, A., et al. Recovery of impenetrable rough surface profiles via CNN-based deep learning architecture. *International Journal of Remote Sensing*, 2022, vol. 43, no. 15–16, p. 5658–5685. DOI: 10.1080/01431161.2022.2105177

[38] KUO, Y. H., KIANG, J. F. Deep-learning linear sampling method for shape restoration of multilayered scatterers. *Progress In Electromagnetics Research C*, 2022, vol. 124, p. 197–209. DOI: 10.2528/PIERC22081005.

[39] BELKEBIR, K., SAILLARD, M. Testing inversion algorithms against experimental data. *Inverse problems*, 2001, vol. 17, no. 6, p. 1565–1571. DOI: 10.1088/0266-5611/17/6/301

[40] FRANCHOIS, A., PICHOT, C. Microwave imaging-complex permittivity reconstruction with a levenberg-marquardtmethod. *IEEE Transactions on Antennas and Propagation*, 1997, vol. 45, no. 2, p. 203–215. DOI: 10.1109/8.560338

[41] PASTORINO, M. *Microwave Imaging*. John Wiley & Sons, 2010. ISBN: 780470278000

[42] PETERSON, A. F., RAY, S. L., MITTRA, R. *Computational Methods for Electromagnetics*. New York: Wiley-IEEE Press, 1998. ISBN: 9780780311220

[43] COLTON, D., HADDAR, H., PIANA, M. The linear sampling method in inverse electromagnetic scattering theory. *Inverse Problems*, 2003, vol. 19, no. 6, p. 105–137. DOI: 10.1088/0266-5611/19/6/057

[44] CATAPANO, I., CROCCO, L., ISERNIA, T. On simple methods for shape reconstruction of unknown scatterers. *IEEE Transactions on Antennas and Propagation*, 2007, vol. 55, no. 5, p. 1431–1436. DOI: 10.1109/TAP.2007.895563

[45] CATAPANO, I., CROCCO, L. An imaging method for concealed targets. *IEEE Transactions on Geoscience and Remote Sensing*, 2009. vol. 47, no. 5, p. 1301–1309. DOI: 10.1109/TGRS.2008.2010773

[46] CATAPANO, I., CROCCO, L., D'URSO, M., et al. 3D microwave imaging via preliminary support reconstruction: Testing on the fresnel 2008 database. *Inverse Problems*, 2009, vol. 25, no. 2, p. 1–23. DOI: 10.1088/0266-5611/25/2/024002

[47] BRIGNONE, M., BOZZA, G., ARAMINI, R., et al. A fully no-sampling formulation of the linear sampling method for threedimensional inverse electromagnetic scattering problems. *Inverse Problems*, 2009, vol. 25, no. 1, p. 1–20. DOI: 10.1088/0266-5611/25/1/015014

[48] JIN, K. H., MCCANN, M. T., FROUSTEY, E., et al. Deep convolutional neural network for inverse problems in imaging. *IEEE Transactions on Image Processing*, 2017, vol. 26, no. 9, p. 4509–4522. DOI: 10.1109/TIP.2017.2713099

[49] RONNEBERGER, O., FISCHER, P., BROX, T. U-net: Convolutional networks for biomedical image segmentation. In *International Conference on Medical Image Computing and Computer-Assisted Intervention (MICCAI)*. Munich (Germany), 2015, p. 234–241. DOI: 10.1007/978-3-319-24574-4_28

[50] ALOM, M. Z., HASAN, M., YAKOPCIC, C., et al. Recurrent residual convolutional neural network based on U-Net (R2U-Net) for medical image segmentation. *arXiv:1802.06955*, 2018, p. 1–12. DOI: 10.48550/arXiv.1802.06955

[51] WEI, Z., CHEN, X. Deep-learning schemes for full-wave nonlinear inverse scattering problems. *IEEE Transactions on Geoscience and Remote Sensing*, 2018, vol. 57, no. 4, p. 1849–1860. DOI: 10.1109/TGRS.2018.2869221

[52] THATHAMKULAM, A. A., BENNY, R., CHERIAN, P., et al. Non-iterative microwave imaging solutions for inverse problems using deep learning. *Progress In Electromagnetics Research M*, 2021, vol. 102, p. 53–63. DOI: 10.2528/PIERM21021304

[53] KHOSHDEL, V., ASHRAF, A., LOVETRI, J. Enhancement of multimodal microwave-ultrasound breast imaging using a deep-learning technique. *Sensors*, 2019, vol. 19, no. 18, p. 1–14. DOI: 10.3390/s19184050

[54] WEI, Z., LIU, D., CHEN, X. Dominant-current deep learning scheme for electrical impedance tomography. *IEEE Transactions on Biomedical Engineering*, 2019, vol. 66, no. 9, p. 2546–2555. DOI: 10.1109/TBME.2019.2891676

[55] HARISHA, S. B, MALLIKARJUN, E., AMIT, M. Deep learning assisted distorted born iterative method for solving electromagnetic inverse scattering problems. *Progress In Electromagnetics Research C*, 2023, vol. 133, p. 65–79. DOI: 10.2528/PIERC23040702

[56] GOODFELLOW, I., BENGOI, Y., COURVILLE, A. *Deep Learning*. MIT Press, 2016. ISBN: 0262035618

[57] KANDEL, I., CASTELLI, M. The effect of batch size on the generalizability of the convolutional neural networks on a histopathology dataset. *ICT Express*, 2020, vol. 6, no. 4, p. 312–315. DOI: 10.1016/j.icte.2020.04.010

About the Authors . . .

Shimoga Beerappa HARISHA (corresponding author) has received his M.Tech. from the National Institute of Technology Warangal in 2009. He is currently pursuing a Ph.D. degree at the National Institute of Technology Goa. His research interests include microwave imaging and inverse problems.

Erramshetty MALLIKARJUN has received his M.Tech. and Ph.D. degrees from the Indian Institute of Technology Kharagpur in 2009 and 2016, respectively. Currently, he is an Assistant Professor with the National Institute of Technology Goa. His fields of interest include microwave imaging, terahertz imaging, and inverse problems.

Magdum AMIT has received his M.Tech. from Walchand College of Engineering Sangli in 2016 and Ph.D. degree from the National Institute of Technology Goa in 2023. His research interests include microwave imaging and inverse problems.